SUPPLEMENTARY INFORMATION

Beyond Ceria: Theoretical Investigation of Isothermal and Near-Isothermal Redox Cycling of Perovskites for Solar Thermochemical Fuel Production

Richard J. Carrillo[a] and Jonathan R. Scheffe[a,*]

[a]*Department of Mechanical and Aerospace Engineering, University of Florida, Gainesville, Florida, 32611, USA*

[*]*Corresponding author. Phone: +1 352-392-0839; Email Address: jscheffe@ufl.edu.*

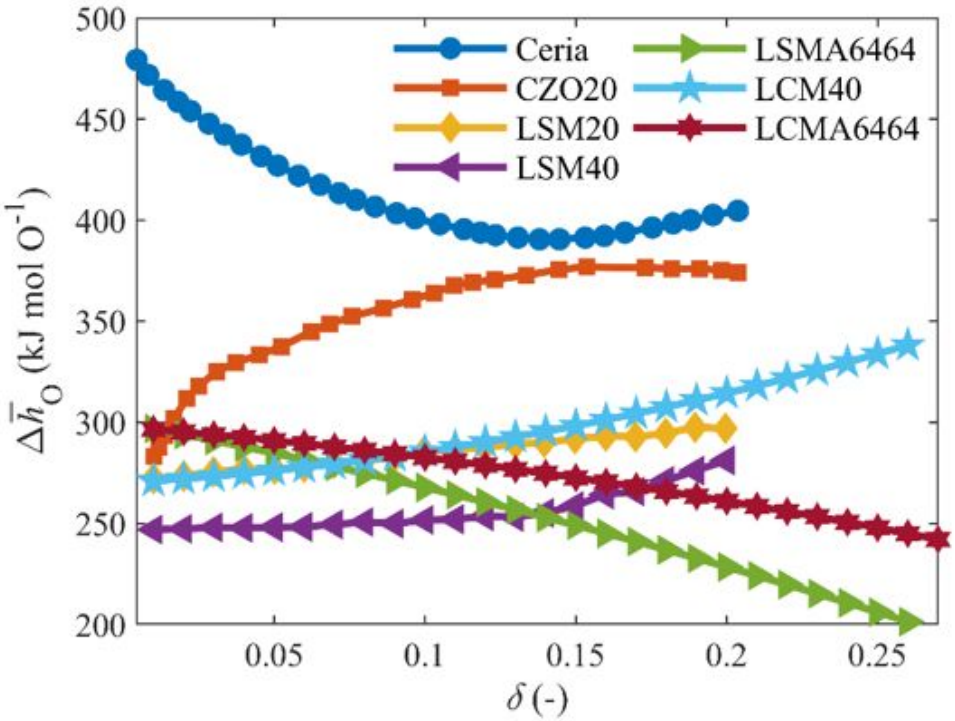

Figure S1. Partial molar enthalpy change per mole of monoatomic oxygen versus nonstoichiometry for each of the materials considered.

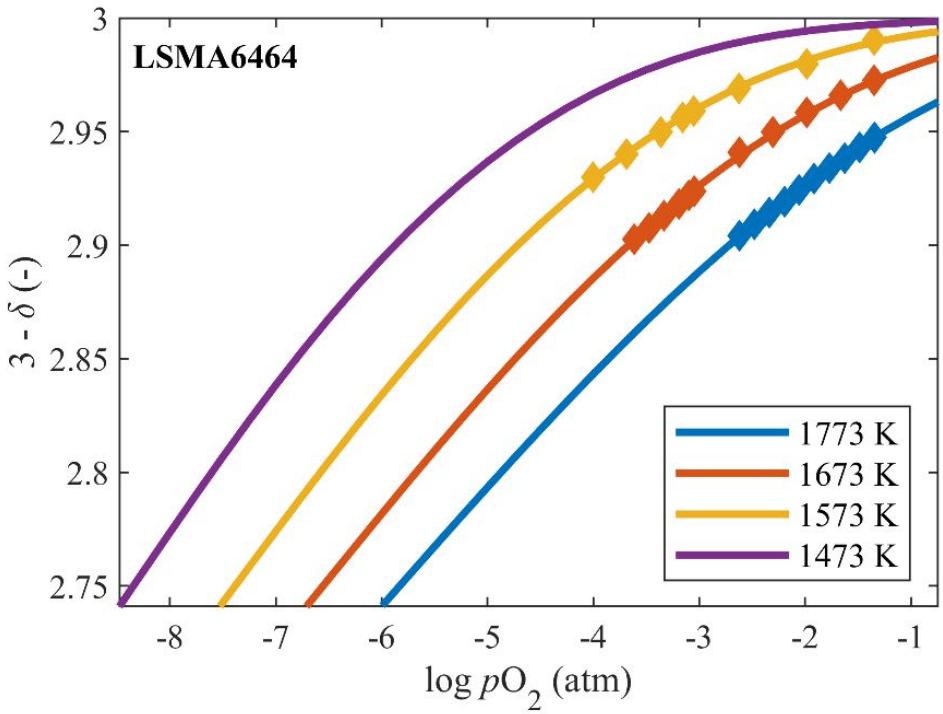

Figure S2. Equilibrium oxygen content of LSMA6464 versus pO_2 at 1473-1773 K. The markers indicate measured data extracted from Takacs *et al.* The solid lines represent defect model fits considering (1) production of doubly ionized oxygen vacancies and reduction of Mn^{4+} to Mn^{3+} and (2) disproportionation of Mn^{3+} to Mn^{4+} and Mn^{2+}.

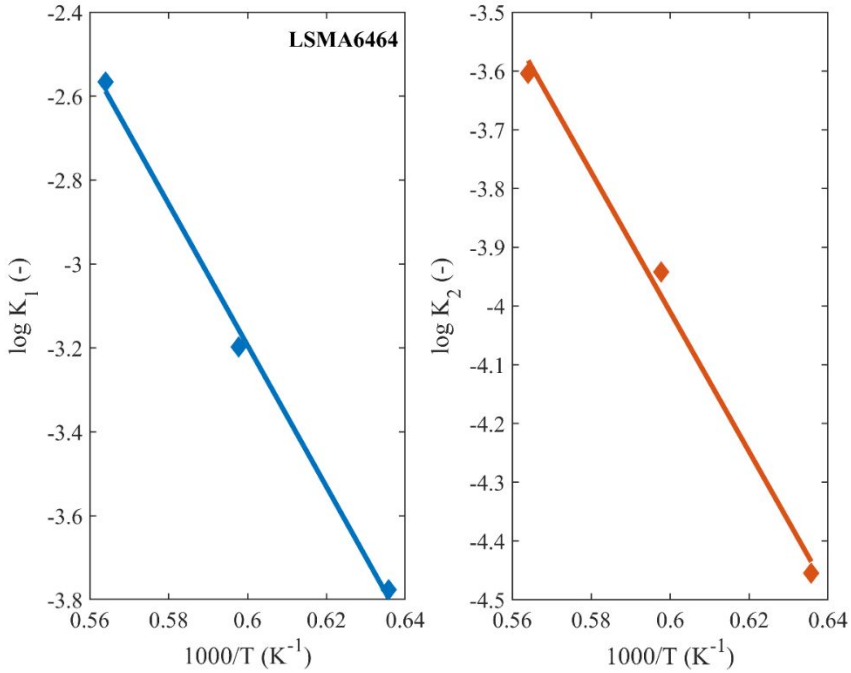

Figure S3. Logarithm of the equilibrium constants of oxygen vacancy formation (K_1) and disproportionation (K_2) versus inverse temperature for LSMA6464. Markers represent the extracted value at a single temperature and the solid lines represent linear fits.

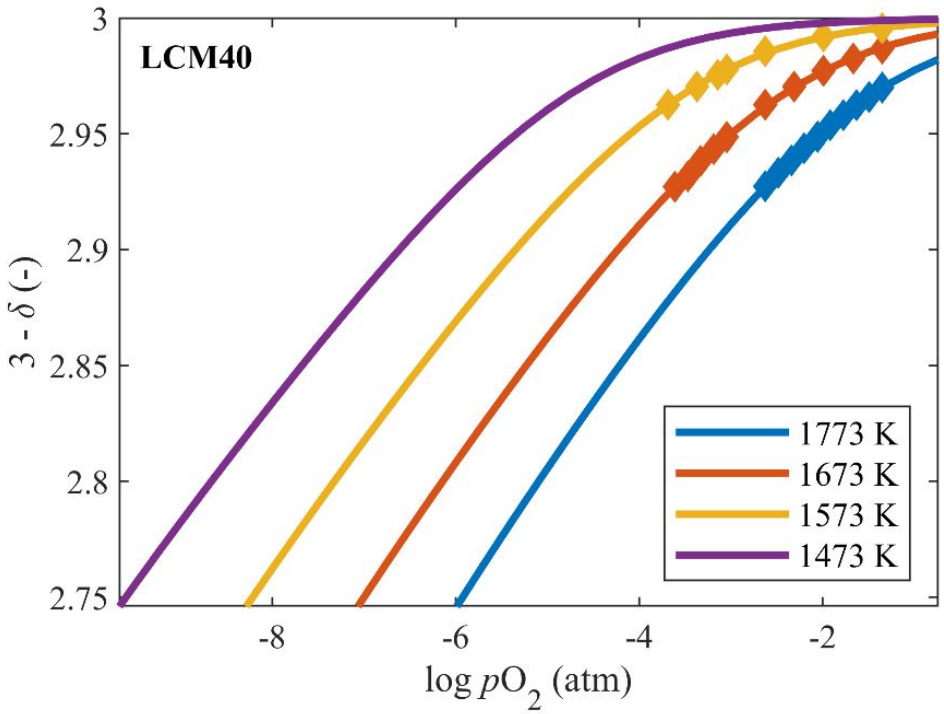

Figure S4. Equilibrium oxygen content of LCM40 versus pO_2 at 1473-1773 K. The markers indicate measured data extracted from Takacs *et al.* The solid lines represent defect model fits considering (1) production of doubly ionized oxygen vacancies and reduction of Mn^{4+} to Mn^{3+} and (2) disproportionation of Mn^{3+} to Mn^{4+} and Mn^{2+}.

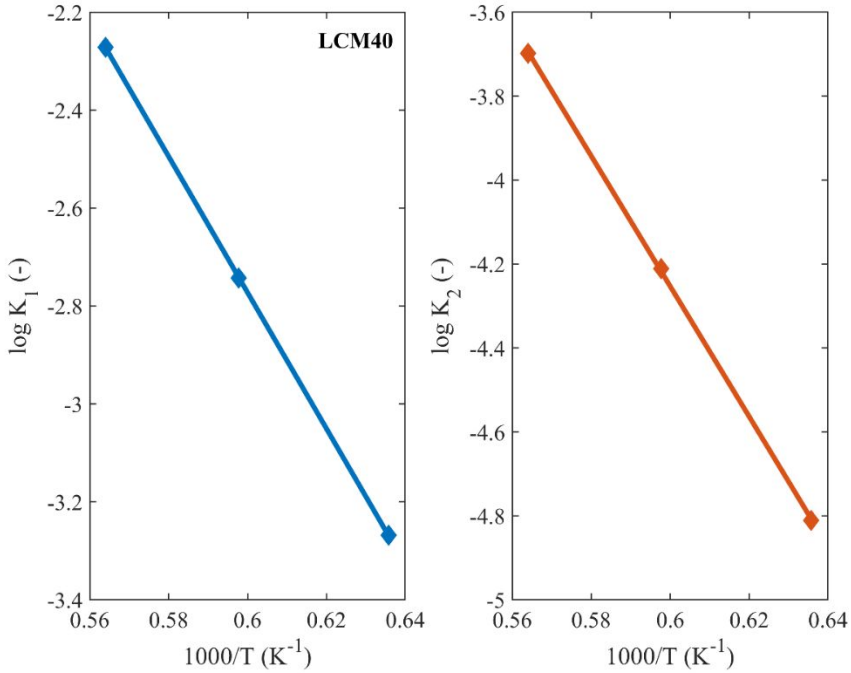

Figure S5. Logarithm of the equilibrium constants of oxygen vacancy formation (K_1) and disproportionation (K_2) versus inverse temperature for LCM40. Markers represent the extracted value at a single temperature and the solid lines represent linear fits.

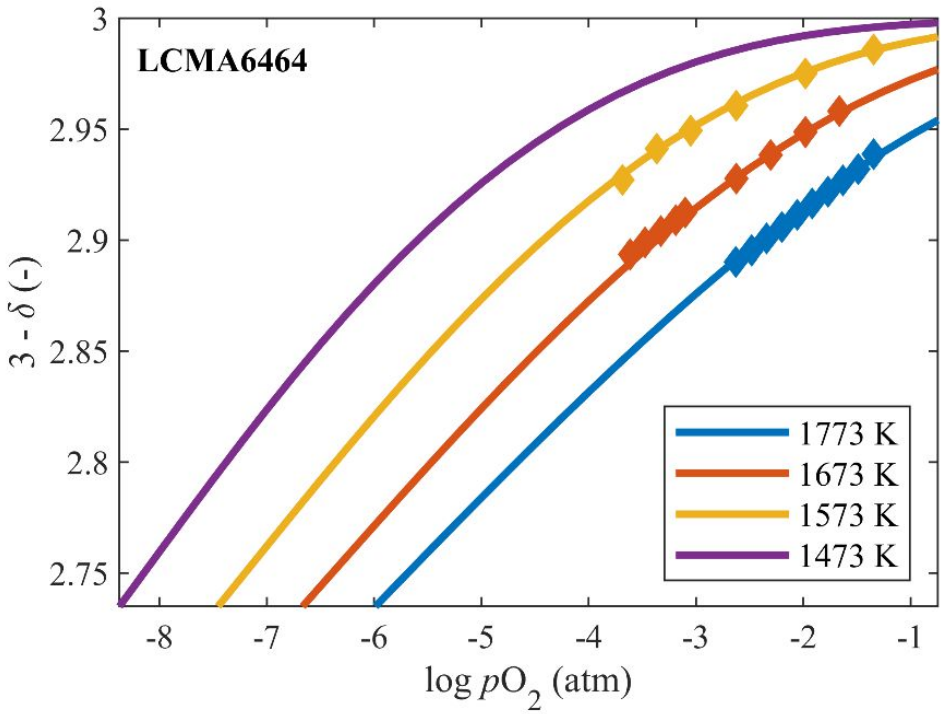

Figure S6. Equilibrium oxygen content of LCMA6464 versus pO_2 at 1473-1773 K. The markers indicate measured data extracted from Takacs *et al.* The solid lines represent defect model fits considering (1) production of doubly ionized oxygen vacancies and reduction of Mn^{4+} to Mn^{3+} and (2) disproportionation of Mn^{3+} to Mn^{4+} and Mn^{2+}.

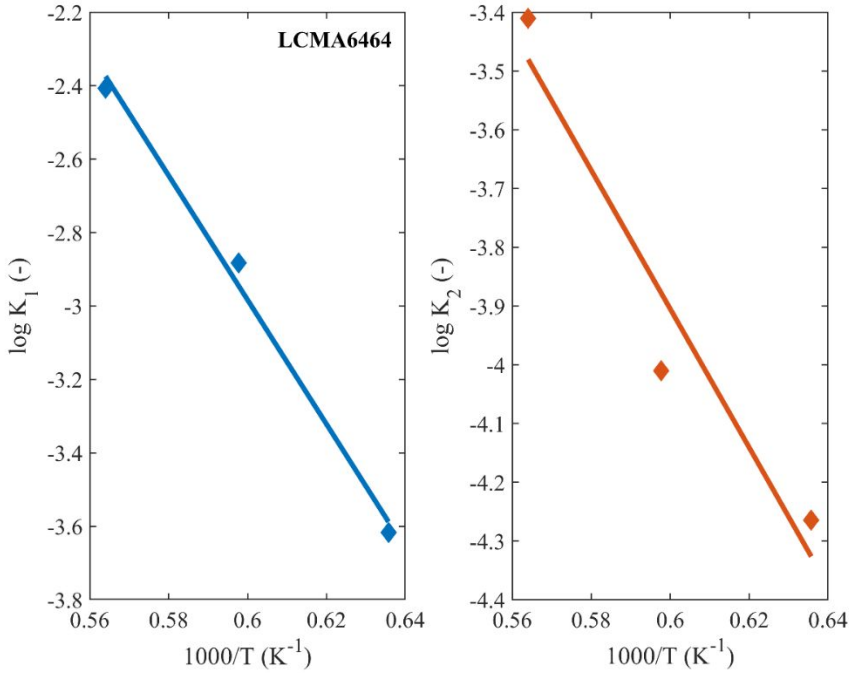

Figure S7. Logarithm of the equilibrium constants of oxygen vacancy formation (K_1) and disproportionation (K_2) versus inverse temperature for LCMA6464. Markers represent the extracted value at a single temperature and the solid lines represent linear fits.

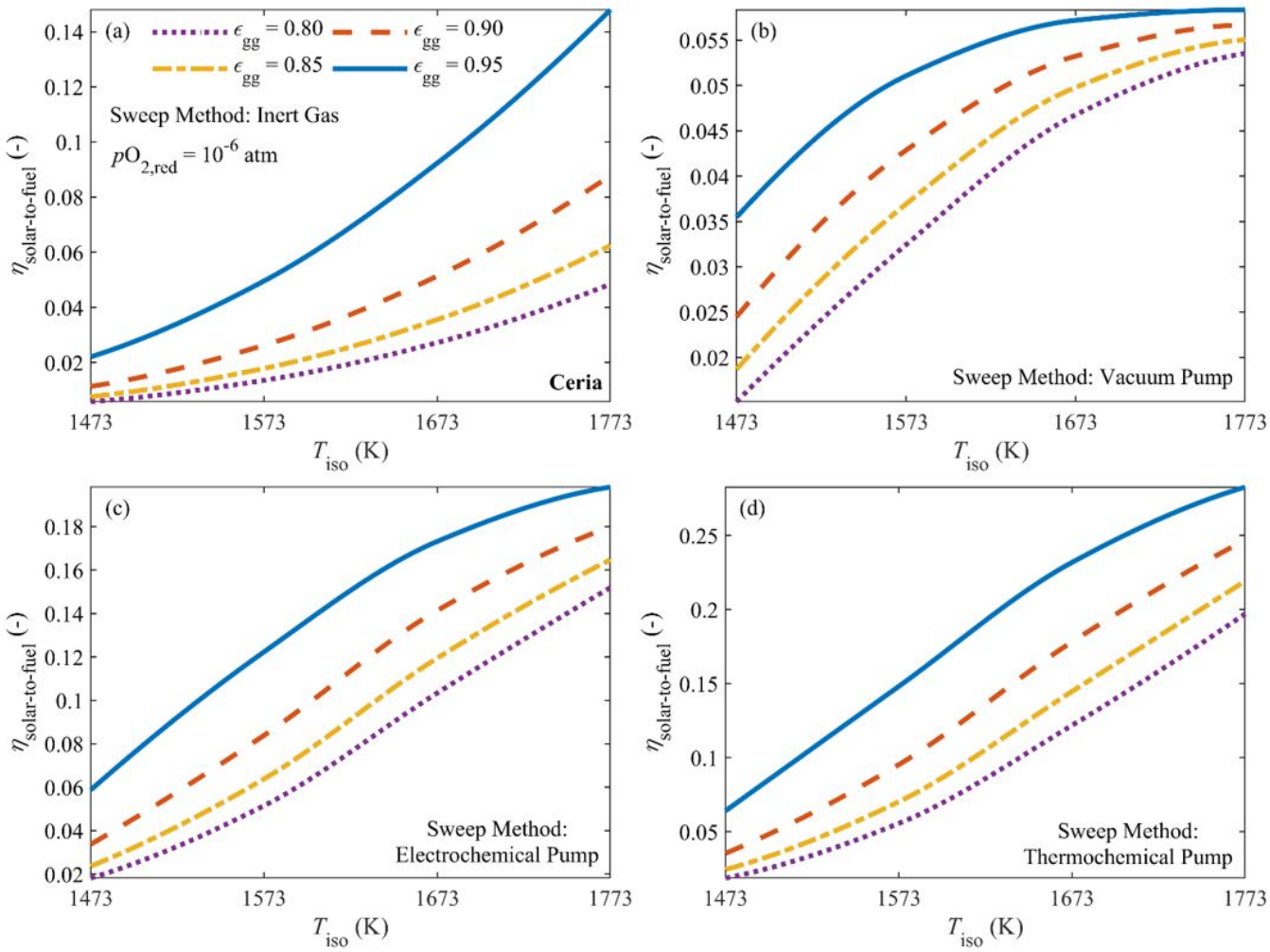

Figure S8. Solar-to-fuel energy conversion efficiencies for H_2O splitting versus operating temperature for isothermal redox cycles using ceria. The reduction pO_2 was 10^{-6} atm and the geometric concentration ratio was 3000. The gas-to-gas heat recovery effectiveness was varied from 0.80 to 0.95. The reduction pO_2 was controlled via (a) inert gas sweeping, (b) a mechanical vacuum pump, (c) an electrochemical oxygen pump, or (d) a thermochemical oxygen pump.

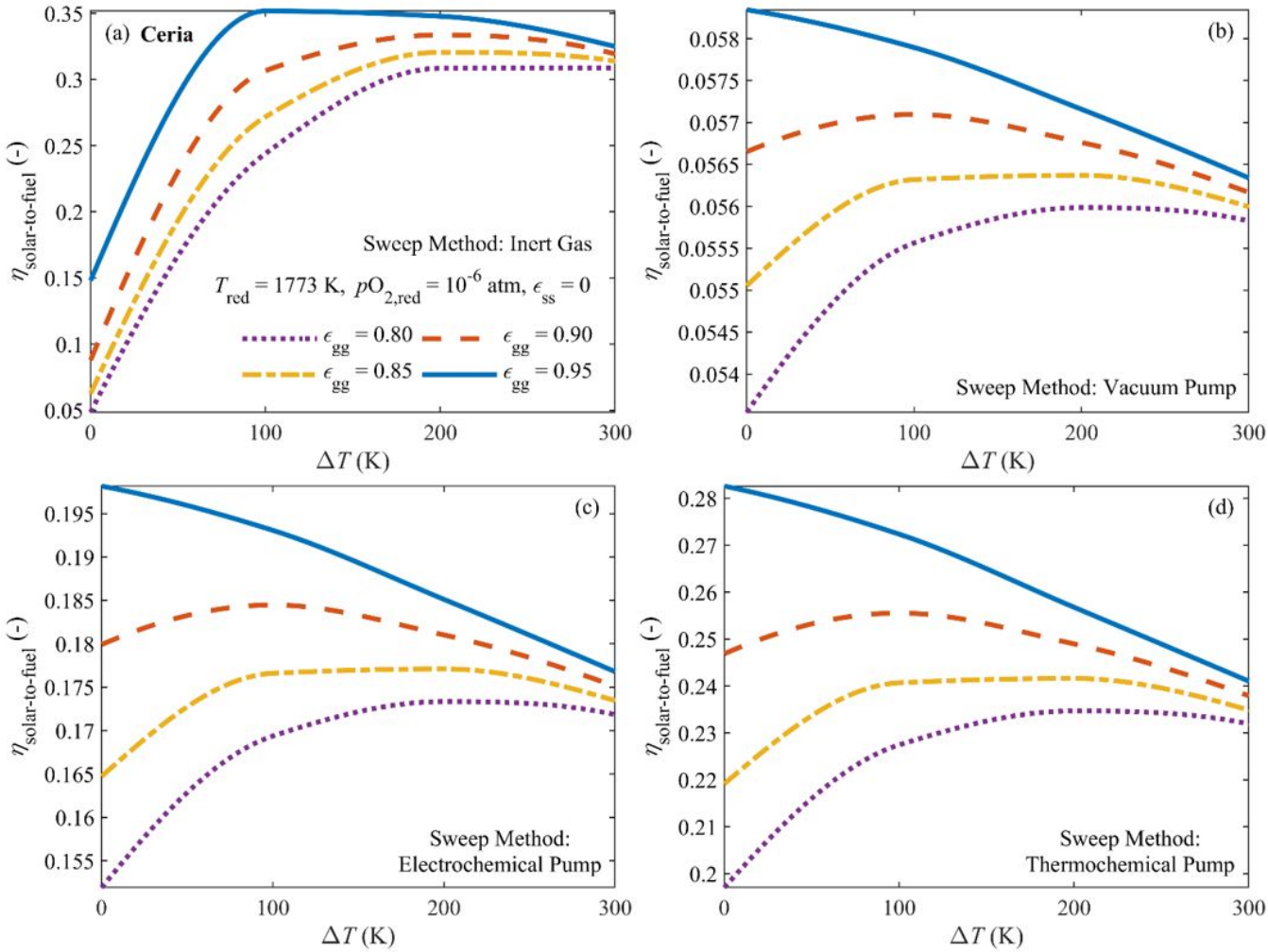

Figure S9. Solar-to-fuel energy conversion efficiencies for H_2O splitting versus temperature swing for nonisothermal redox cycles using ceria. The reduction pO_2 was 10^{-6} atm, zero solid-to-solid heat recovery was considered, and the geometric concentration ratio was 3000. The gas-to-gas heat recovery effectiveness was varied from 0.80 to 0.95. The reduction pO_2 was controlled via (a) inert gas sweeping, (b) a mechanical vacuum pump, (c) an electrochemical oxygen pump, or (d) a thermochemical oxygen pump.

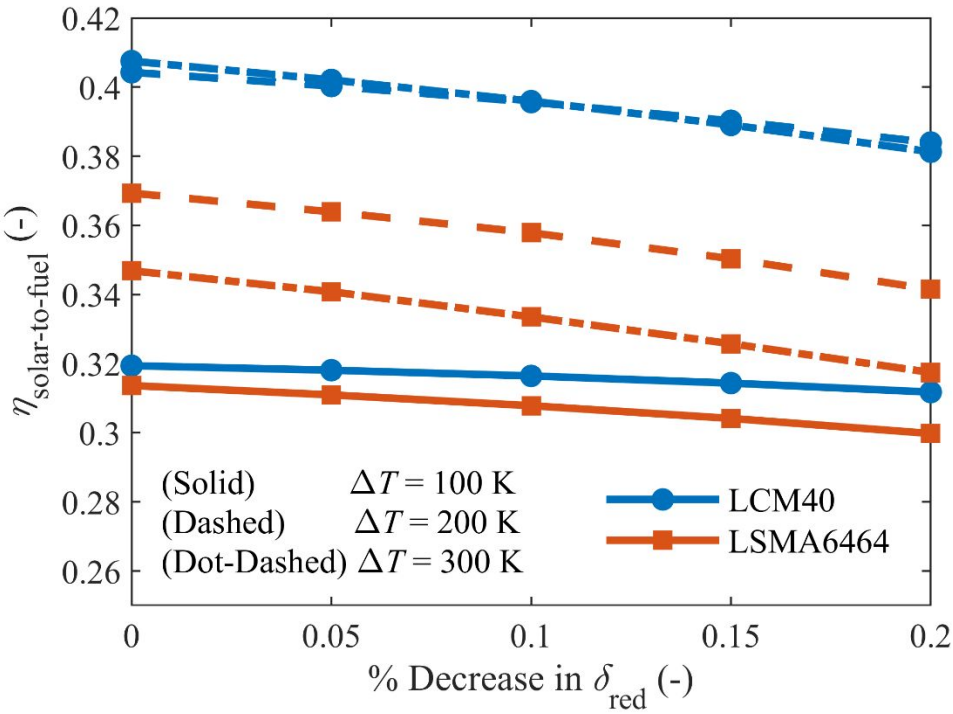

Figure S10. Sensitivity analysis showing $\eta_{\text{solar-to-fuel}}$ versus an assumed percent decrease in δ_{red} for TSRC with LCM40 and LSMA6464.